First-principles determination of the effects of intermolecular interactions on the electronic transport through molecular monolayers

Luis A. Agapito, Chao Cao, and Hai-Ping Cheng
Department of Physics and Quantum Theory Project, University of Florida, Gainesville, Florida 32611, USA
(Received 27 May 2008; published 15 October 2008)

We extend our previous development of electron transport through one-dimensional (1D) molecular junctions to two-dimensional (2D) monolayers. Our methodology calculates the tunneling current through a single molecule that is embedded in an infinite 2D monolayer of such molecules self-assembled on gold and covered on top also with gold. In this way, the intermolecular interactions that take place between neighboring molecules are fully accounted for within the accuracy of the density-functional theory. As application examples, we study monolayers of nitro substituted oligo phenylene-ethynylene (nitroOPE) dithiol molecules. Monolayers with the packing density observed experimentally are compared against others with lower density, in which the intermolecular interactions are negligible. Additionally, two different adsorption sites (hollow and atop) are considered for the nitroOPE. The results show that the effect of the intermolecular interactions on the tunneling current depends heavily on the adsorption site of the molecule. Hollow-site-adsorbed monolayers undergo a dramatic reduction in current due to the intermolecular interactions, whereas the change in atop-site-adsorbed monolayers is minimal.

DOI: 10.1103/PhysRevB.78.155421 PACS number(s): 73.50.−h, 85.65.+h, 85.35.−p, 73.63.−b

I. INTRODUCTION

Ideally a one-dimensional (1D) molecular junction is composed of a single molecule (or a few of them that can still be treated as a single molecule) attached to two perfect semi-infinite 1D wires. Ideal 1D junctions are exactly solvable models within the single-particle, mean-field-type approximation, such as the one implied in density-functional theory (DFT). Within this approximation, the problem of electron transport through these ideal 1D junctions presents a formally "exact" solution when the exact surface Green's function (SGF) of the leads is used.[1–3] However, experimental realization of ideal 1D junctions, and thus direct comparison to the calculations, has difficulties such as manipulation of individual wires (i.e., carbon nanotubes), or positioning of a single molecule between them. Although catalytically grown nanowires may be easier to build into 1D junctions, they usually have cross sections too large to be simulated by current computational techniques. Additionally, 1D junctions cannot capture the two-dimensional (2D) periodicity of most experimental settings. Because of the irremediable mismatch to experimental settings, generally, 1D models are not endued to quantitatively reproduce the experiments.

The stability and robustness of thiol-OPE-based self-assembled monolayers (SAMs) have propelled important experimental observations of their electronic properties such as switching between on/off states of conductance,[4,5] reproducible memory effects, and negative differential resistance (NDR).[6–8] Common experimental settings (crossed-wire,[9] in-wire,[10,11] or nanopore[12]) consider junctions where the leads have large contact areas. These experiments address monolayers of self-assembled molecules, where intermolecular interactions are present, rather than isolated molecules.[13,14] This is especially true for OPE thiols and derivatives such as the nitroOPE considered here, which assembles in highly ordered patterns with typical domains of about 100 Å.[15]

Therefore, a two–dimensional (2D) model is more suitable for comparison to experimental settings rather than a 1D one, in the sense that they include the effect of a single molecule surrounded by neighboring ones. 2D models facilitate the study of phenomena originated by intermolecular interactions.[16,17] For instance, packing densities of thiol-mediated SAMs have been shown to strongly influence the energetic alignment between substrate and adsorbate with a drastic change in the electron transport properties being expected.[18] Also, it has been recently reported that NDR features may be due to intermolecular interactions.[19]

Analogous to 1D junctions, ideal 2D junctions also allow for an "exact" solution; however, unlike their 1D counterparts, ideal 2D junctions can better capture the geometrical periodicities and the chemistry of the experimental settings. Nonetheless, there are unknowns in the experimental junctions such as percentage of coverage, surface reconstruction, impurities and pinhole effects, bond formation, etc. that may still prevent a direct comparison with the theoretical predictions.

Although vastly most electronic transport calculations are performed as 1D models, the use of periodicity in the direction transverse to transport (2D) has also been considered, especially in the study of bulk magnetic materials[20,21] or extended basis sets,[22] but considerably less in the context of molecular crystals using localized basis sets.[16,17,23,24]

We extend our previous development[1] to the case of electron transport through 2D molecular junctions. As application examples, the current through nitroOPE molecules in the absence and presence of intermolecular interactions is calculated. We also test the dependence of those interactions with respect to the molecular adsorption sites (atop and hollow).

II. MODELING UNIT CELLS AND PARAMETERS

The self-assembly of thiol-terminated organic molecules on Au (111) surfaces occurs with the sulfur adsorbing on top

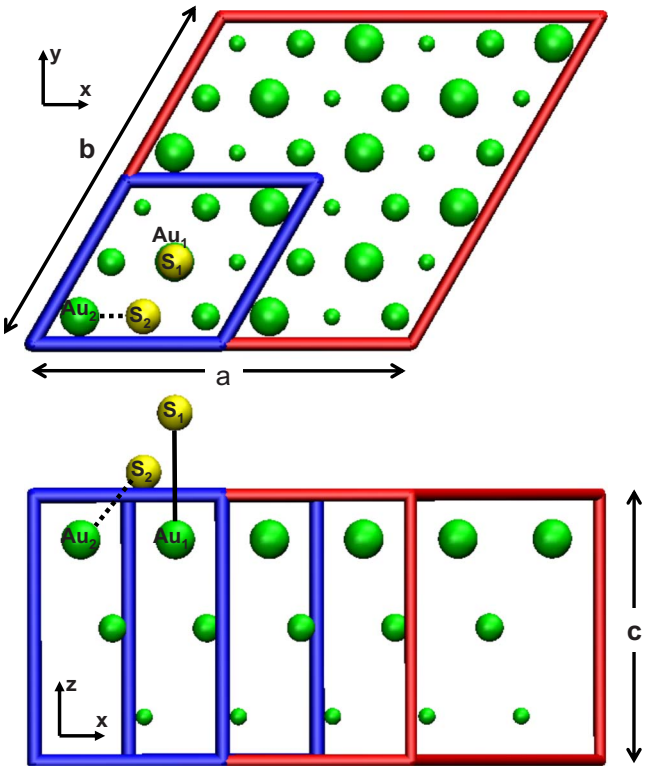

FIG. 1. (Color online) Top and front view of modeling unit cells for Au bulk. The z axis aligns to the Au [111] crystallographic direction. The shortest Au-Au bond in the first layer is 2.88 Å and the interlayer separation 2.35 Å. The sulfur atoms (yellow) pinpoint the positions through which the nitroOPE (not shown) adsorbs on the first Au layer (bigger green atoms). The red and blue unit cells correspond to the cases of lightly and densely packed adsorption, with surface cells $(2\sqrt{3}\times 2\sqrt{3})R30°$ and $(\sqrt{3}\times\sqrt{3})R30°$ Au (111), respectively. Atop- and hollow-site adsorption are considered. In the atop-site adsorption, the nitroOPE connects perpendicularly to the Au surface through a thiol bond S_1-Au_1 of length 3.36 Å. In the hollow adsorption, the mediating sulfur (S_2) is equally distant to the three nearest Au atoms, with S_2-Au_2 bond equal to 2.44 Å. The parameters of the red cell are $a=b=9.99$ Å, $c=7.06$ Å, $\alpha=90°$, $\beta=90°$, and $\gamma=60°$.

of either a Au atom (atop, S_1 in Fig. 1), the Au-Au bond (bridge), or the hollow site of a Au-Au-Au triangle (hollow, S_2 in Fig. 1); hollow-site adsorption is the most stable conformation and atop the least.[25] In the present study we consider only FCC-hollow-site adsorption with a S_2-Au_2 bond of 2.44 Å, and atop-site adsorption with a S_1-Au_1 distance of 3.36 Å, according to previous findings.[26]

In order to assess the effect of intermolecular interaction, two different molecular packing densities are studied. In the case of high packing density, we position one molecule per $(\sqrt{3}\times\sqrt{3})R30°$ Au (111) cell; this cell is consistent with estimations from atomic force microscopy (AFM) (Ref. 27) and scanning tunneling microscopy (STM) (Ref. 15) images and is shown demarked in blue in Fig. 1. The other case corresponds to junctions with low packing densities, in which the molecules are positioned further separated from each other as to avoid molecular interactions; in this case, we have one molecule per $(2\sqrt{3}\times 2\sqrt{3})R30°$ Au (111) cell, demarked in red in Fig. 1.

In total, we consider four molecular junctions that span two different adsorption sites and two packing densities. Each junction is composed of an infinite 2D molecular monolayer in between two semi-infinite Au crystals. Junction 2 is composed of a densely packed monolayer of nitroOPE molecules adsorbed on an atop site; the modeling cell for junction 2 is shown in Fig. 3(a). In junction 3, whose modeling cell is shown in Fig. 3(b), the nitroOPE is adsorbed on a hollow site and the monolayer is only lightly packed. The remaining junctions 1 and 4, which are not shown, correspond to the cases of lightly packed atop and densely packed hollow conformations, respectively.

The top gold lead is built to be symmetric to the bottom lead, within a small in-plane displacement to reflect the backbone bending of the nitroOPE. In the present comparative study, we only consider adsorption of the nitroOPE perpendicular to the substrate. For all cases the geometry of the molecule and gold layers are fixed.

All the electronic structure calculations are performed under the DFT implemented in the SIESTA package.[28] We use the DFT Perdew-Burke-Ernzerhof (PBE) functional[29] and localized basis sets of single-ζ quality for the valence electrons; the core electrons are represented by pseudopotentials generated using the Troullier-Martins scheme. The basis set is constructed based on pseudoatomic orbitals with confining radii determined by an energy shift of 0.02 Ry.[30,31]

III. METHODOLOGY

The electronic structure information is obtained from two separate DFT calculations. The first calculation simulates Au bulk using three-dimensional (3D) periodic boundary conditions (PBCs), and the other simulates the device region using 2D PBCs on the modeling cells shown in Fig. 1. The electronic structure of the molecular junction is found by integrating the information from both DFT calculations through the Green's function formalism.

A. Gold bulk

We choose the hexagonal cell shown in Fig. 1 (blue) as the unit cell for the DFT 3D calculation of the Au bulk. Repeating such a unit cell in the x-y plane, spanned by the unit vectors $\vec{a}$ and $\vec{b}$, generates a 2D infinite Au (111) slab and stacking them in the z direction reproduces the bulk. The electronic structure information of the Au bulk, in the form of Hamiltonian matrices $H_{\mathbf{0R}_n}$, is obtained from the DFT 3D calculation using special Monkhorst-Pack[32] $6\times 6\times 6$ **k** points and other settings described above. The site-space Hamiltonian matrix $H_{\mathbf{0R}_n}$ represents the interaction between cell **0** (in layer 0) and a cell located at a generic position **R** within layer n, as depicted in Fig. 2(a). Since **R** pinpoints the discrete positions of the cells rather than continuous coordinates, we refer to it as site-space coordinates instead of real-space ones.

$H_{\mathbf{0R}_1}$ is a function of **R**, describing the interaction between cell **0** in layer 0 and any cell **R** that belongs to layer 1. The standard forward discrete Fourier transform (FDFT) of such a function over the x-y plane is

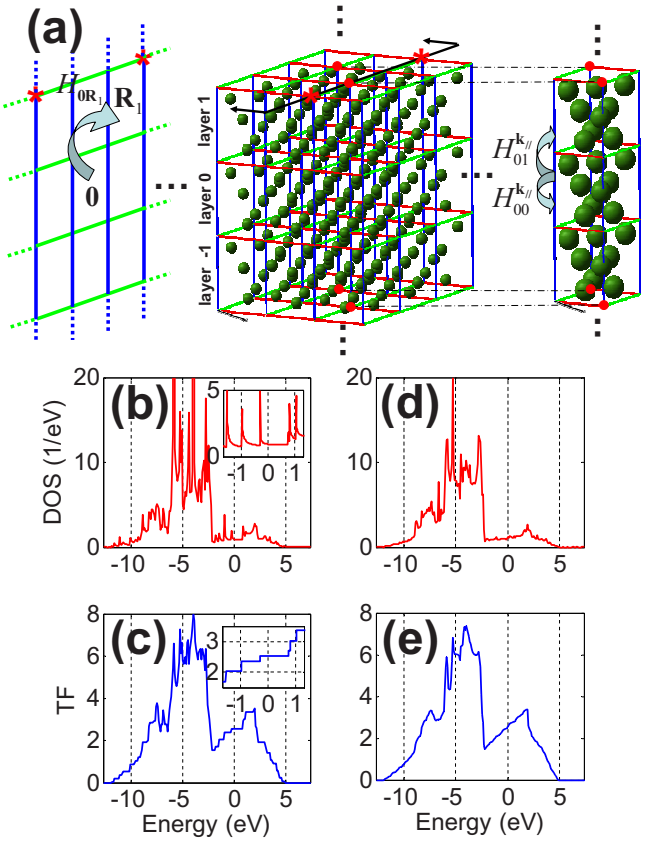

FIG. 2. (Color online) (a) Middle: Representation of Au bulk seen as a stack of infinite layers. Left: The schematic cross section shows the interactions between the central cell **0** in layer 0 and a generic cell $\mathbf{R}_1$ that belongs to layer 1. Right: In Fourier space, each layer of the Au bulk is folded into a site of an infinite wire. (b) and (c) are the DOS and TF for the Au bulk calculated using 6×6 $\mathbf{k}_\parallel$ points. (d) and (e) correspond to the DOS and TF of Au bulk calculated using 20×20 $\mathbf{k}_\parallel$ points. The Fermi level is set to 0 eV.

$$H_{01}^{\mathbf{k}_\parallel} = \sum_{\mathbf{R}\in\text{layer }1} e^{i\mathbf{k}_\parallel\cdot\mathbf{R}} H_{0\mathbf{R}_1}, \tag{1}$$

where $\mathbf{k}_\parallel$ is a vector, with $k_z=0$, in the reciprocal space of $\{\vec{a},\vec{b},\vec{c}\}$. The negative sign in the exponential drops because of the symmetry of the lattice. Analogously, the FDFT of $H_{0\mathbf{R}_0}$, the coupling between cell **0** in layer 0 and any cell **R** that belongs to layer 0, is

$$H_{00}^{\mathbf{k}_\parallel} = \sum_{\mathbf{R}\in\text{layer }0} e^{i\mathbf{k}_\parallel\cdot\mathbf{R}} H_{0\mathbf{R}_0}. \tag{2}$$

The hopping matrix $H_{01}^{\mathbf{k}_\parallel}$ is the interaction between two consecutive infinite layers for a given wave vector $\mathbf{k}_\parallel$; $H_{00}^{\mathbf{k}_\parallel}$ is the on-site interaction within a layer. The size of both matrices is equal to the number of basis functions in the Au unit cell; thus, mathematically, we can consider that each layer folds into a site of an infinite 1D wire, which extends from $\pm\infty$ in the z direction, as depicted in Fig. 2(a). Also, it can be interpreted that, in Fourier space, the problem of a 3D Au bulk is converted into several problems of a "1D wire."

In the *ab initio* tight-binding (TB) approximation, the process of finding the electronic and transport properties of 1D wires only requires the information of the hopping $H_{01}^{\mathbf{k}_\parallel}$ and the on-site $H_{00}^{\mathbf{k}_\parallel}$ matrices (and their corresponding overlap matrices $S_{01}^{\mathbf{k}_\parallel}$,$S_{00}^{\mathbf{k}_\parallel}$).[33,34] The TB approximation is satisfactory as long as the next-to-nearest-neighbor interactions ($H_{02}^{\mathbf{k}_\parallel}$, $H_{03}^{\mathbf{k}_\parallel}$, etc.) are negligible; in principle, they can be tuned to be small by increasing the thickness of the Au unit cell. For our chosen unit cell and SIESTA's default Au confining radius, the next-to-nearest-neighbor interactions are exactly zero in the DFT calculation; therefore, we do not incur any loss of accuracy, with respect to the DFT calculation, when invoking the TB approximation.

The Green's function $G_0^{\mathbf{k}_\parallel}$ of the perfectly infinite "1D wire" and the surface Green's functions for the left ($G_L^{0\mathbf{k}_\parallel}$) and right ($G_R^{0\mathbf{k}_\parallel}$) semi-infinite wires, obtained by splitting the infinite wire, are calculated as described elsewhere:[1,33]

$$G_0^{\mathbf{k}_\parallel}(E) = \{[H_{01}^{\mathbf{k}_\parallel} - ES_{01}^{\mathbf{k}_\parallel}][(\alpha_<^{\mathbf{k}_\parallel})^{-1} - \beta_>^{\mathbf{k}_\parallel}]\}^{-1}, \tag{3}$$

$$G_L^{0\mathbf{k}_\parallel}(E) = \alpha_<^{\mathbf{k}_\parallel}[H_{01}^{\mathbf{k}_\parallel} - ES_{01}^{\mathbf{k}_\parallel}]^{-1}, \tag{4}$$

$$G_R^{0\mathbf{k}_\parallel}(E) = \beta_>^{\mathbf{k}_\parallel}[(H_{01}^{\mathbf{k}_\parallel})^\dagger - E(S_{01}^{\mathbf{k}_\parallel})^\dagger]^{-1}, \tag{5}$$

where the matrices $\alpha_<^{\mathbf{k}_\parallel}$ and $\beta_>^{\mathbf{k}_\parallel}$ are obtained in the same way and notation described in Eqs. (29), (32), and (13) of Ref. 1. The density of states (DOS) $\text{DOS}_0^{\mathbf{k}_\parallel}$ and transmission function (TF) $\text{TF}_0^{\mathbf{k}_\parallel}$ of the perfect wire are given by

$$\text{DOS}_0^{\mathbf{k}_\parallel} = \text{Tr}\left[-\frac{1}{\pi}\text{Im}(G_0^{\mathbf{k}_\parallel}S_{00}^{\mathbf{k}_\parallel})\right], \tag{6}$$

$$\text{TF}_0^{\mathbf{k}_\parallel} = \text{Tr}(\Gamma_L^{\mathbf{k}_\parallel}G_0^{\mathbf{k}_\parallel}\Gamma_R^{\mathbf{k}_\parallel}G_0^{\mathbf{k}_\parallel\dagger}), \tag{7}$$

where

$$\Gamma_{L/R}^{\mathbf{k}_\parallel} = i[\Sigma_{L/R}^{\mathbf{k}_\parallel} - (\Sigma_{L/R}^{\mathbf{k}_\parallel})^\dagger], \tag{8}$$

$$\Sigma_L^{\mathbf{k}_\parallel}(E) = (H_{01}^{\mathbf{k}_\parallel} - ES_{01}^{\mathbf{k}_\parallel})^\dagger G_L^{0\mathbf{k}_\parallel}(H_{01}^{\mathbf{k}_\parallel} - ES_{01}^{\mathbf{k}_\parallel}),$$

$$\Sigma_R^{\mathbf{k}_\parallel}(E) = (H_{01}^{\mathbf{k}_\parallel} - ES_{01}^{\mathbf{k}_\parallel})G_R^{0\mathbf{k}_\parallel}(H_{01}^{\mathbf{k}_\parallel} - ES_{01}^{\mathbf{k}_\parallel})^\dagger. \tag{9}$$

In order to obtain any of the above properties in site space rather than in $\mathbf{k}_\parallel$ reciprocal space, the corresponding inverse discrete Fourier transform (IDFT) is performed. Since we are interested in the density of states of the central cell or the transmission function through the central cell ($\mathbf{R}=\mathbf{0}$), the IDFT is reduced to

$$\text{DOS}_0(E) = \frac{1}{N}\sum_{\mathbf{k}_\parallel} e^{i\mathbf{k}_\parallel\cdot\mathbf{R}}\text{DOS}_0^{\mathbf{k}_\parallel} = \frac{1}{N}\sum_{\mathbf{k}_\parallel}\text{DOS}_0^{\mathbf{k}_\parallel}, \tag{10}$$

where N is the number of $\mathbf{k}_\parallel$ points used. $\text{DOS}_0^{\mathbf{k}_\parallel}$ can be considered as the density of states of a Au unit cell that is immersed in an infinite wire. The summation through all $\mathbf{k}_\parallel$ points adds the interaction with all other neighboring infinite wires; therefore, the initial unit cell is truly embedded in an infinite 3D bulk and DOS_0 is nothing but the density of states of Au bulk.

For calibration purposes, the DOS of the gold bulk is calculated using two different $\mathbf{k}_\parallel$ meshes in the FDFT. As seen in Figs. 2(b) and 2(c), the use of an insufficient number

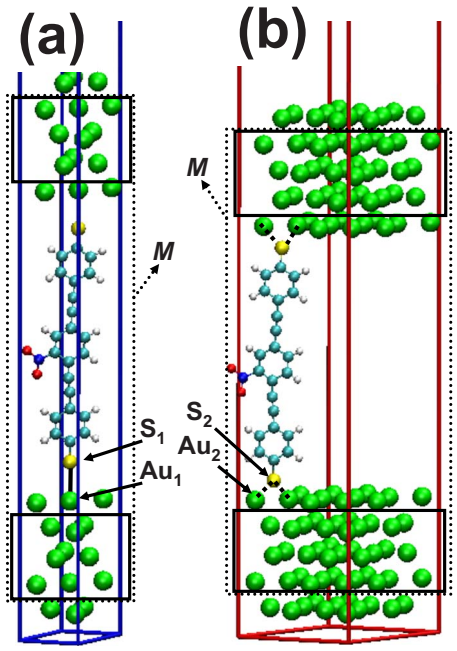

FIG. 3. (Color online) Unit cells used in the DFT 2D calculations corresponding to the (a) densely and (b) lightly packed junctions. (a) illustrates atop-site adsorption (solid black S_1-Au_1 lines) whereas (b) a hollow-site one. For the hollow-site adsorption, sulfurs are equally bonded to three nearest Au atoms (dashed black S_2-Au_2 lines; the third bond and neighboring Au atom are not shown). Dotted rectangles demark the device regions (M) and solid ones the unit cells used to reproduce the Au bulk and obtain the different surface Green's functions needed. Bond lengths are given in Fig. 1.

of $\mathbf{k}_\parallel$ (6×6) introduces unphysical sharp peaks in the density of states, which reflect in unrealistic step-wise features in the transmission function around the Fermi level. The use of 6×6 $\mathbf{k}$ points for the x-y plane is satisfactory in the DFT 3D calculation since the Born–von Karman boundary condition[35–38] is suitable for the wave function, i.e., it is likely to be periodic after crossing a macrocell of 6×6. However, error is introduced when using the same mesh for FDFT-ing $H_{\mathbf{0R}_1}$ and $H_{\mathbf{0R}_0}$ in Eqs. (1) and (2), since those functions clearly decay with $\mathbf{R}$; thus, they are aperiodic. In the FDFT of an aperiodic function it is necessary to enlarge the size of the macrocell under Born–von Karman conditions to avoid including fictitious periodicities; that is, performed by increasing the number of $\mathbf{k}_\parallel$ points to 20×20, which eliminates the nonphysical features in the density of states and transmission function, as seen in Figs. 2(d) and 2(e).

B. Molecular junctions

Strictly, the device region is also 2D infinite; but, hereafter only a unit cell (denoted by M) will be referred to as the device region, demarked by dotted rectangles in Fig. 3. In order to simulate molecular junctions, we need to add the effect of the top and bottom semi-infinite Au bulk to the device region. Because of the x-y periodicity of the junctions, this is done in a per $\mathbf{k}_\parallel$ point, per unit-cell basis, correcting the Hamiltonian matrix ($H_M^{\mathbf{k}_\parallel}$) of the device region with the self-energy for the bottom and top gold contacts; see Eq. (9). The Green's function for the device region is

$$G_M^{\mathbf{k}_\parallel}(E) = [ES_M^{\mathbf{k}_\parallel} - H_M^{\mathbf{k}_\parallel} - \Sigma_L^{\mathbf{k}_\parallel}(E) - \Sigma_R^{\mathbf{k}_\parallel}(E)]^{-1}. \tag{11}$$

$H_M^{\mathbf{k}_\parallel}$ and $S_M^{\mathbf{k}_\parallel}$ are the FDFTs of site-space coupling and overlap matrices ($H_{\mathbf{0R}}$,$S_{\mathbf{0R}}$),

$$H_M^{\mathbf{k}_\parallel} = \sum_{\mathbf{R}} e^{i\mathbf{k}_\parallel\cdot\mathbf{R}} H_{\mathbf{0R}},$$

$$S_M^{\mathbf{k}_\parallel} = \sum_{\mathbf{R}} e^{i\mathbf{k}_\parallel\cdot\mathbf{R}} S_{\mathbf{0R}}. \tag{12}$$

In this case, $H_{\mathbf{0R}}$ (and $S_{\mathbf{0R}}$) is obtained from the DFT 2D calculation (using $6\times6\times1$ $\mathbf{k}$ points) of the modeling cells and represents the interaction between the device regions (only) of both cell $\mathbf{0}$ and cell $\mathbf{R}$; contrary to the DFT 3D calculation for the Au bulk, here $\mathbf{R}$ lies only in the plane spanned by $\vec{a}$ and $\vec{b}$. As seen in Fig. 3, the modeling cell is composed of the device region M and extra layers of gold, which are used to mitigate the effect of the long-range Coulomb interactions from the bulk. $H_{\mathbf{0R}}$ is built by disregarding the matrix elements corresponding to those extra layers.

The TF through the device region is calculated according to Caroli's formula,[39]

$$\mathrm{TF}^{\mathbf{k}_\parallel} = \mathrm{Tr}(\Gamma_L^{\mathbf{k}_\parallel} G_M^{\mathbf{k}_\parallel} \Gamma_R^{\mathbf{k}_\parallel} G_M^{\mathbf{k}_\parallel\dagger}). \tag{13}$$

For further analysis it is useful to determine the contribution of any given subset of atoms (fragment) to the total density of states. The projected density of states (PDOS) on such a fragment is calculated by summing up some components of the main diagonal of the Green's function matrix, according to the following definition (see the Appendix):

$$\mathrm{PDOS}_{\mathrm{fragment}}^{\mathbf{k}_\parallel} \equiv \sum_{\forall\, b\in\mathrm{fragment}} \left[-\frac{1}{\pi}\mathrm{Im}(G_M^{\mathbf{k}_\parallel} S_M^{\mathbf{k}_\parallel}) \right]_{bb}$$

$$\approx \sum_{\forall\, b\in\mathrm{fragment}} \left[-\frac{1}{\pi}\mathrm{Im}(S_M^{\mathbf{k}_\parallel} G_M^{\mathbf{k}_\parallel} S_M^{\mathbf{k}_\parallel}) \right]_{bb}, \tag{14}$$

where the index b represents any basis function used in the representation of the atoms that belong to the chosen fragment. The total DOS of the device region is

$$\mathrm{DOS}_M^{\mathbf{k}_\parallel} = \mathrm{Tr}\left[-\frac{1}{\pi}\mathrm{Im}(G_M^{\mathbf{k}_\parallel} S_M^{\mathbf{k}_\parallel}) \right]. \tag{15}$$

Within the linear-response approximation, we calculate the current of electrons as

$$I^{\mathbf{k}_\parallel} = \frac{2e}{h}\int_{-\infty}^{+\infty} dE \mathrm{TF}^{\mathbf{k}_\parallel}(E, V=0)[f(E-\mu_R) - f(E-\mu_L)]. \tag{16}$$

The bias-voltage drop is considered to be applied from the bottom ($L+$) to the top ($R-$); thus, a positive value of current signifies electrons traveling from the top to bottom contact.

Again, the properties in site space (G_M, DOS_M, PDOS, TF, I) are obtained from the IDFT with $\mathbf{R}=\mathbf{0}$. The Au bulk

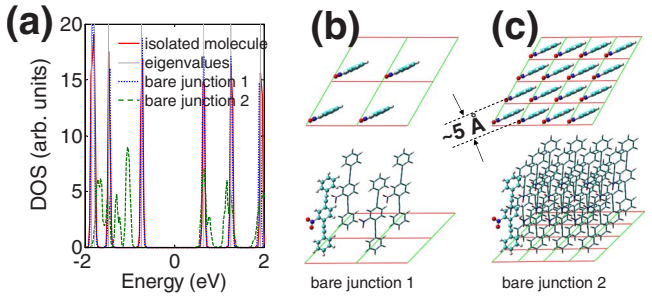

FIG. 4. (Color online) Junctions of bare nitroOPE molecules; they do not include gold or sulfur atoms. The packing densities of the bare junctions 1 (b) and 2 (c) match those of junctions 1 and 2; their DOSs are shown in blue (dotted line) and green (dashed line), respectively. The red curve (solid line) is the DOS of an isolated single molecule and the vertical gray lines the Kohn-Sham energy levels. Unlike the other cases, these DOS plots are obtained directly from broadening the eigenvalues by 0.03 eV.

calculation imposes the limiting constraint in the fineness of the $\mathbf{k}_\parallel$ mesh; we use the same mesh (20×20 $\mathbf{k}_\parallel$ points) for the calculation of the molecular junctions.

We point out that DOS_M is in fact the density of states of a single molecule (more accurately the device region M) that is both (1) embedded within an infinite 2D self-assembly, thus feeling the influence of their neighbors. The information of intermolecular interactions is contained in the $H_{00}^{\mathbf{k}_\parallel}$ and $H_{01}^{\mathbf{k}_\parallel}$ matrices, which are generated from the DFT 2D calculation, and (2) sandwiched between a bottom and a top gold slab which are effectively of infinite thickness. The finite-thickness slabs that are considered as part of the device region are made effectively infinite by correcting the Hamiltonian with the exact self-energies in Eq. (9). Unless otherwise indicated, all PDOS and DOS presented in this study are calculated as the IDFT of Eq. (14) or Eq. (15).

IV. RESULTS AND DISCUSSION

A. Bare monolayers

Preliminarily, we calculate two monolayers of bare molecules built to match the low and high packing densities of junction 1 and junction 2, respectively. The bare monolayers do not include gold or sulfur atoms and are shown in Figs. 4(b) and 4(c). The DOSs for both (bare monolayers 1 and 2) are given in Fig. 4(a) (blue and green, respectively); additionally, the DOS (red) and eigenvalues (gray) of an isolated nitroOPE molecule are included for comparison. All DOS curves in Fig. 4(a) are obtained directly from SIESTA, by broadening the eigenvalues 0.03 eV.

The agreement between the DOS peaks of bare junction 1 (blue) and those of the isolated molecule (red) corroborates that the intermolecular interactions in junction 1 are negligible. On the other hand, the DOS of bare junction 2 (green) exhibits broadening of the lowest unoccupied molecular orbital (LUMO) and shifting of the highest occupied molecular orbital (HOMO) by −0.3 eV; the deviation from the red peaks corroborates the presence of intermolecular interactions, which lead to the formation of energy bands between

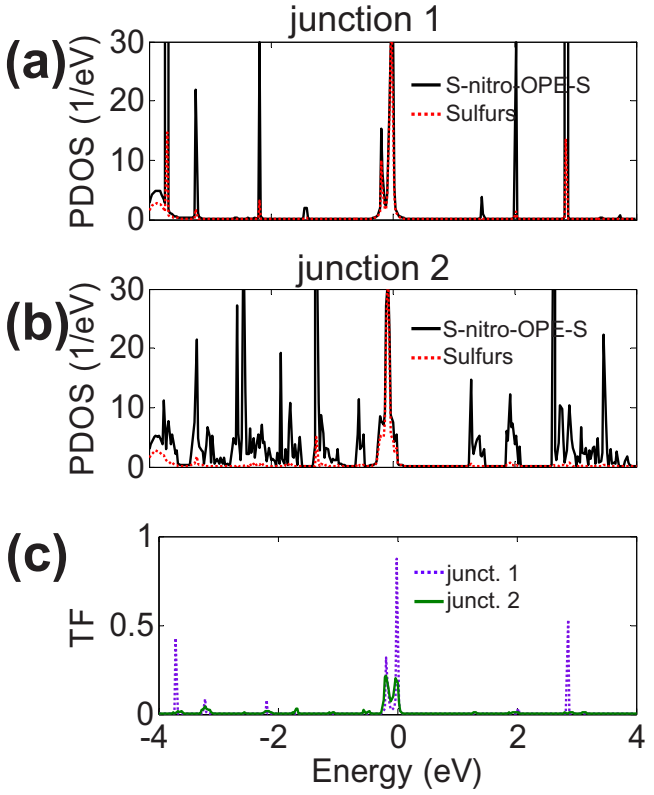

FIG. 5. (Color online) DOS projected on the S-nitroOPE-S fragment, for junction 1 (a) and junction 2 (b), black curves (solid lines); the DOS projections on sulfurs are shown in red (dotted lines). (c) Comparison of the transmission functions at 0 V for both junctions. The Fermi levels of the junctions are set to 0 eV.

molecular energy levels. Then, we affirm that our choice of test systems covers the cases of the absence and presence of intermolecular interaction. For consistency in comparing junctions of different packing densities, we do not consider the herringbone pattern for the high-density SAMs;[15,27,40] instead, all molecules are positioned parallel, as seen in Figs. 4(b) and 4(c).

B. Atop-site adsorption

In the case of atop adsorption, at a S-to-Au-surface distance of 3.36 Å, the S-nitroOPE-S is only weakly coupled to the top and bottom contacts. Furthermore, in junction 1 the molecules are also far separated from each other, effectively being isolated. This is evidenced by the sharp peaks in the S-nitroOPE-S PDOS [Fig. 5(a), black]; moreover, these peaks readily match to the eigenenergies (at the Γ point) of the DFT 2D calculation of the modeling cell, as shown in Fig. 6.

We turn on the intermolecular interactions by doubling the packing density of the SAM (junction 2); the presence of interactions is verified by the formation of new bands (peaks) and broadening and shifting of the original peaks [Fig. 5(b), black]. A similar tendency is found for the junctions with hollow-site adsorption when the intermolecular interactions are turned on [Fig. 7(a) against Fig. 7(b)].

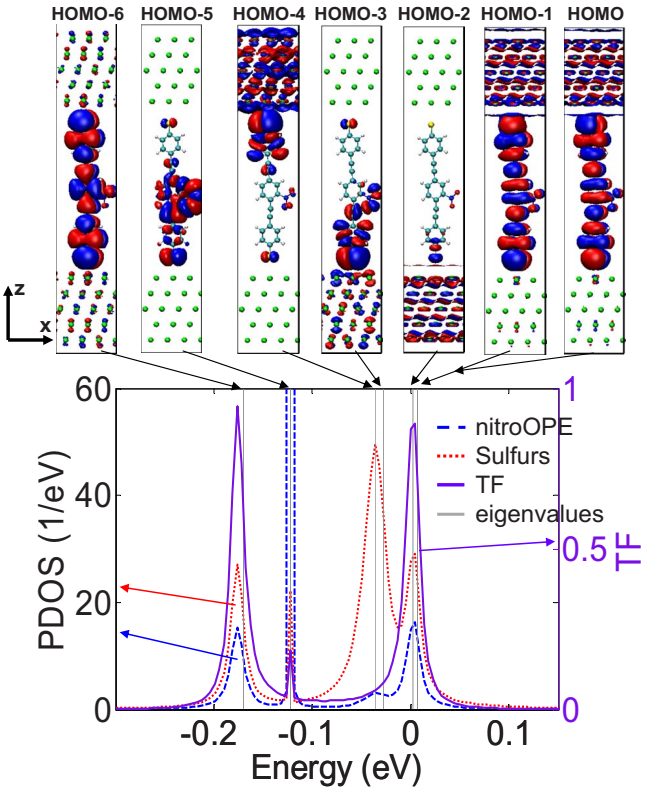

FIG. 6. (Color online) Zoom in of Fig. 5(a) (dotted red line), around the Fermi level, calculated using a larger number of energy points. The nitroOPE PDOS (dashed line) is the difference between black and red curves in Fig. 5(a). The denser energy mesh allows the observation of new features, such as the sharp HOMO-5 peak. All the molecular orbitals correspond to an isosurface of 0.03. The value of the Fermi level of the junction is subtracted from all eigenvalues.

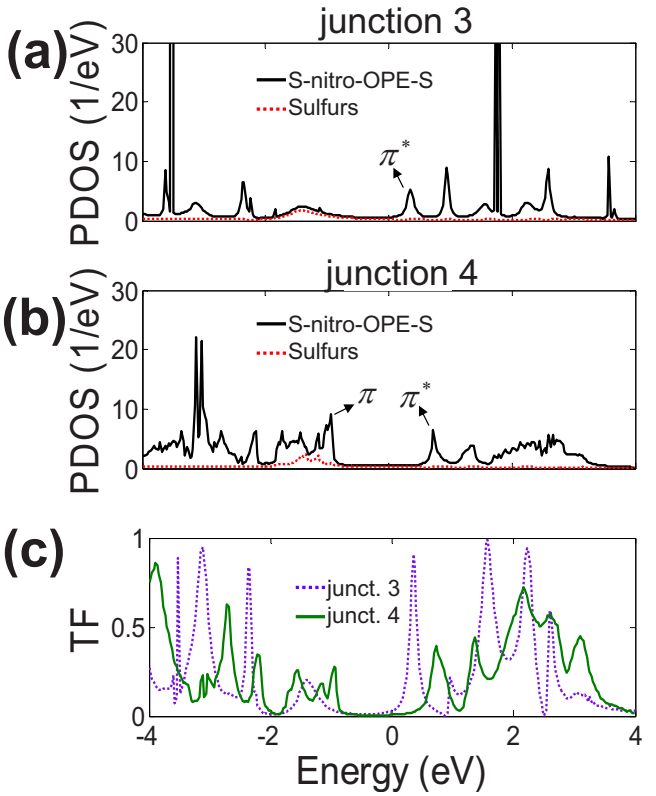

FIG. 7. (Color online) S-nitroOPE-S PDOSs for junctions 3 (a) and 4 (b), black curves (solid lines); the S PDOSs are shown in red (dotted). (c) Transmission functions at 0 V for both junctions. The Fermi levels are set to 0 eV.

The S-nitroOPE-S PDOS reveals a peak aligned right at the Fermi level of the junction [Fig. 5(a), black]. At first sight, this resonant peak appears to be facilitated almost entirely by the electronic states of the sulfur atoms [Fig. 5(a), red] and has been observed for monolayers of thiol-terminated molecules with weak S-metal hybridization.[26]

Figure 6 zooms in around the Fermi level region of Fig. 5(a). For clarity, the nitroOPE PDOS (blue) is shown instead of the S-nitroOPE-S PDOS; the Γ-point eigenenergies are marked by vertical gray lines. The use of a higher number of energy points in Fig. 6, compared to Fig. 5(a), reveals the presence of additional peaks, which clearly match the eigenenergies.

As shown in Fig. 6, the [HOMO-3, HOMO-4] peak is mainly due to the sulfurs, not the nitroOPE. This translates, in real space, in electrons delocalizing along the sulfurs but not the nitroOPE and corresponds to a broken channel for conduction, which is confirmed by the corresponding zero transmission function. On the other hand, the [HOMO, HOMO-1, HOMO-2] peak is contributed almost equally by both the nitroOPE and sulfurs, increasing the probability to form, in real space, a continuous channel throughout the junction, similar to the delocalization seen in the corresponding molecular orbitals.

The [HOMO-5] peak is very sharp with a corresponding sharp contribution to the transmission function. The composition of the [HOMO-6] peak resembles that of the [HOMO, HOMO-1, HOMO-2] peak; consequently, both peaks show a similar contribution to the transmission function.

The presence of S PDOS peaks indicates the preservation of the atomic character of sulfurs due to weak hybridization with Au; accordingly, orbitals of p_x and p_y character can be seen localized on the sulfurs. For the case of HOMO-6, HOMO-1, and HOMO, those orbitals integrate to the population on the nitroOPE to form a seamless π network throughout S-nitroOPE-S.

C. FCC hollow-site adsorption

Even though junction 1 and junction 3 have the same low packing density, the S-nitroOPE-S PDOS peaks of junction 3 are less sharp than of junction 1. This is due to the stronger interaction between the S-nitroOPE-S and the surface; for hollow-site adsorption (junction 3) the S-to-Au-surface distance is 1.78 Å, against 3.36 Å for the case of atop adsorption (junction 1). Similarly, the S PDOS peaks observed in the atop-adsorbed junctions are smudged over a broad energy window because of the stronger hybridization with gold (S-Au=2.44 Å), as shown by the red curves in Fig. 7.

As seen in Fig. 7(b) (black curves), the S-nitroOPE-S PDOS of junction 4 shows a pseudogap region, which is a band gap with a minimal density of intragap states, around

the Fermi level. Band gaps are characteristic features of semiconductor materials. The frontier peaks of this pseudogap [−0.93 and 0.72 eV in Fig. 7(b), black] and those of the bare junction 2 [−1.03 and 0.65 eV in Fig. 4(a), green] can clearly be traced back to the HOMO and LUMO of the isolated molecule [Fig. 4(a), black]. It is not always straightforward to associate those peaks to particular MOs of the isolated molecule; then, more generally such peaks will be referred to as frontier π and π^* states hereafter.[41] Generally, π and π^* states are delocalized and characteristic frontier states of a phenyl-based system.

For phenyl-based bare monolayers, intragap states have been shown to appear due to intermolecular π overlap,[42–44] i.e., overlapping benzene rings of two neighboring molecules. For separations less than ~3 Å the gap could even be filled and the bare monolayer becomes metallic, allowing ballistic transport parallel to the surface. However, for separations of ~5 Å [as for our case, see Fig. 4(c)], this source of intragap states is negligible.[42] Accordingly, our calculations find that intragap states in junction 4 are contributions entirely from the sulfurs [Fig. 7(b), red] and also the gold leads (not shown) but not from the nitroOPE.

The absence of nitroOPE-induced intragap states indicates that, even for this highly packed case, the intermolecular π overlap is too weak to induce metallic behavior and thus, no transport in the plane of the nitroOPE film. Electronically, junction 4 resembles a metal-semiconductor-metal interface, with the nitroOPE film being the semiconducting region and the Au/S atoms the metallic region.

The U shape in the PDOS [Fig. 7(b), black] is characteristic of metal-semiconductor interfaces, being caused by intragap states induced by the metal.[45] In real space, the intragap states are due to the tails of evanescent metallic wave functions. Electrons travel ballistically from deep inside the bulk to the interface, tunnel across the surface Au/S interface, and then decay exponentially into the nitroOPE region. From the zero transmission function [Fig. 7(c), green] around the pseudogap, it follows that the top-to-bottom and bottom-to-top evanescent wave functions decay totally before they meet, frustrating the formation of a wave function delocalized across the junction that could favor electron tunneling.

As seen by the correspondence between the PDOS and TF peaks in Fig. 7, resonant tunneling is the main transport mechanism. The conduction is mainly through the frontier π^* state; the frontier π states start contributing to conduction at voltages higher than ~2 V.

D. Current-voltage

For the atop adsorption, doubling the packing density produces only small changes in current [Fig. 8(a)]; nonetheless, the junction with hollow-site adsorption undergoes a major reduction in current [~13 times; see Fig. 8(b)] when doubling the packing density of the monolayer. This abrupt change in current can be clearly attributed to the shift of the frontier π^* state peak to a higher energy away from the Fermi level, as seen in Fig. 7, which is caused by the intermolecular interactions.

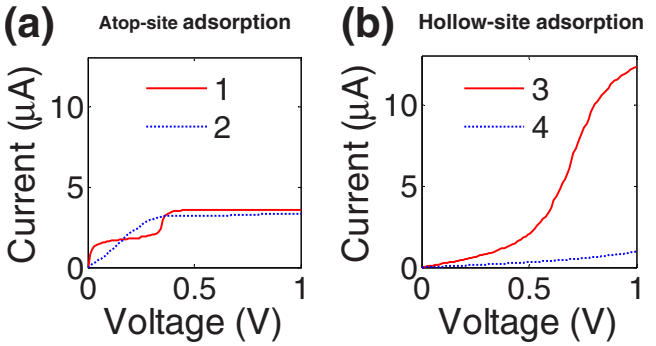

FIG. 8. (Color online) Electrical current per molecule for the four systems considered: junction 1 (atop-site light packing), junction 2 (atop-site dense packing), junction 3 (hollow-site light packing), and junction 4 (hollow-site dense packing).

Of a counterintuitive nature is the fact that, under the same packing density, the current through the physically bound junction 2 is higher than that through the chemically bound junction 4. This counterintuitive higher current has been observed upon stretching similar thiol-mediated junctions[46–48] and is justified by the resonant PDOS peak that appears right at the Fermi level of the junction. Interestingly, the resonant peak shows up only in the limit of very weak coupling to the gold leads (junctions 1 and 2).

According to the plane-averaged charge profile of the junctions, seen in Fig. 9, the Au-molecule interface in junction 1 (atop adsorption) exhibits a more capacitive nature (less sharing of electrons, ionic bond) than junction 3 (hollow adsorption), which presents a more covalent interface (more sharing of electrons). The charge polarization of the thiol bonds in the capacitive case yields an electric dipole (D) layer. Dipole layers induce a sudden jump (assuming no thickness for the dipole layer) in electrostatic-potential profiles. In other words, in an ideal capacitive coupling, the only interaction between the Au surface and the organic SAM

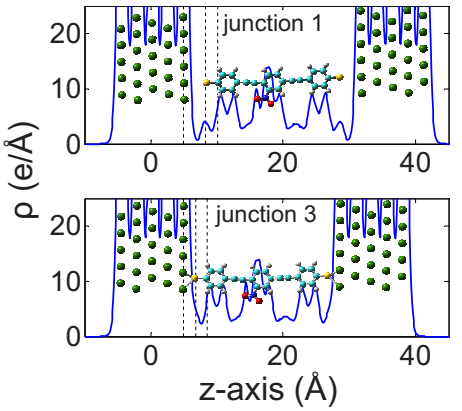

FIG. 9. (Color online) Plane-averaged electron density (valence electrons) along the axis longitudinal to transport for atop (junction 1) and hollow (junction 3) adsorption. Top: The small sharing of electrons within the Au-S interface indicates the more ionic nature of the adsorption (capacitive coupling). Bottom: A larger sharing of electrons is observed between the Au-S planes, indicating covalent bonding. Green, yellow, and cyan represent Au, S, and C atoms, respectively.

would be a block shift of their energy levels (only one degree of freedom); all the eigenenergies of the organic molecule are shifted by a constant number. Then, in junctions with ideal capacitive couplings, the Fermi level alignment can be simply modeled by

$$E_{f\text{junction}} = \text{HOMO}_{\text{S-nitroOPE}} - eD. \tag{17}$$

The highly capacitive nature of the interfaces with atop adsorption is responsible for the direct alignment, Eq. (17), of the work function of the S-nitroOPE-S molecule (HOMO, PDOS peak) to the Fermi level of the gold leads.

This is clearly visible in Fig. 6, where the frontier π state of the S-nitroOPE-S (HOMO) aligns with the Fermi level of the junction. The resonant alignment is responsible for the almost perfect transmission probability observed (TF$\sim$1) at the Fermi level and explains the counterintuitive high current predicted for physically adsorbed thiol-based junctions.

V. SUMMARY AND CONCLUSIONS

We have extended our previous development on electron transport through 1D junctions to handle transport through 2D molecular junctions, which take into account the intermolecular interactions of the type experienced by a molecule embedded in a 2D monolayer. Allowed by the x-y periodicity of the system, the calculation is performed in Fourier space per each $\mathbf{k}_\parallel$ point. Since the SGF of the gold contacts is determined exactly, the solution of the transport problem is also formally exact.

It is important to select an adequate number of $\mathbf{k}_\parallel$ points and not directly assume it to be equal to the number used for the DFT 3D calculation. The use of 6×6 $\mathbf{k}_\parallel$ points introduces spectral leakage that is reflected on the unphysical peaks in the Au-bulk DOS and the corresponding steplike features in the transmission function. We find a good convergence to the correct Au-bulk DOS when using 20×20 $\mathbf{k}_\parallel$ points.

For the molecule under consideration, the effect of the intermolecular interactions on the electronic transport depends on the type of adsorption. For hollow-site adsorption, the presence of neighboring molecules drastically reduces the current by a factor of $\sim$13 with respect to the isolated molecule, whereas for atop-site adsorption, the change in current is only small.

The main mechanism for electron transport in all the junctions in consideration is resonant tunneling perpendicular to the monolayer; the intermolecular distance between phenyl rings is not close enough to induce electron transport parallel to the surface. For the atop-site adsorbed junctions, the transport is mainly facilitated by the frontier π state, which aligns to the Fermi level of the junction. Instead, the transport in the hollow-site adsorbed junctions is mainly through the frontier π^* state. The alignment of the frontier π state to the Fermi level of the junctions explains the counterintuitive high current calculated for the stretched junctions (1 and 2).

ACKNOWLEDGMENTS

We acknowledge the support of the U.S. Department of Energy under Contract No. DOE-FG02-02ER45995 and the computational resources provided at NERSC and HPC@UF. We also thank Hendrik Monkhorst, Magnus Paulsson, Mike Ford, Alexandre Rocha, and Yong-Hoon Kim for several technical discussions.

APPENDIX

Having a closed system, let us define $\hat{G}$ as the Green's function operator, $\bar{G}$ as a Green's function matrix in the space spanned by the nonorthogonal basis set ϕ, $\tilde{G}$ as a Green's function matrix in the space spanned by the orthogonal basis set $\tilde{\phi}$, and G as the Green's function matrix as defined in this paper and commonly in the literature, $G=(ES-H)^{-1}$, with H as the Hamiltonian matrix in the space spanned by the nonorthogonal basis ϕ. S is the overlap matrix such that $S_{ij}=\langle\phi_i|\phi_j\rangle$.

The relationships between those Green's function matrices are known to be[49–51]

$$\tilde{G} = GS,$$

$$\bar{G} = SGS. \tag{A1}$$

The relation between the orthogonalized ($\tilde{\phi}$) and the nonorthogonal (ϕ) basis set is given by the nonunitary transformation $S^{-1/2}$ as follows:

$$\tilde{\phi}_b = \sum_\nu (S^{-1/2})_{\nu b}\phi_\nu. \tag{A2}$$

Although the total DOS is proportional to the trace of the Green's function matrix $\bar{G}$, there is not a unique relation for the projection on each basis (each diagonal element or subsets of them). The problem is analogous to splitting the total charge of a molecule into each basis function; there is no correct procedure but only conventionally accepted schemes. At the end, when summed over atoms, all the different schemes should yield similar atomic charges.

Thus, we can define per-basis function DOS projections using either an orthogonal ($\tilde{\phi}_b$) or nonorthogonal (ϕ) basis as follows:

$$\text{PDOS}_{\tilde{\phi}_b} \equiv -\frac{1}{\pi}\text{Im}(\tilde{G})_{bb},$$

$$\text{PDOS}_{\phi_b} \equiv -\frac{1}{\pi}\text{Im}(\bar{G})_{bb}. \tag{A3}$$

Using Eq. (A1), we obtain

$$\text{PDOS}_{\tilde{\phi}_b} \equiv -\frac{1}{\pi}\text{Im}(\tilde{G})_{bb} = -\frac{1}{\pi}\text{Im}(GS)_{bb}, \tag{A4}$$

$$\text{PDOS}_{\phi_b} \equiv -\frac{1}{\pi}\text{Im}(\bar{G})_{bb} = -\frac{1}{\pi}\text{Im}(SGS)_{bb}. \tag{A5}$$

For a more chemical analysis, it may be desirable to use Eq. (A5), which is the projection on the original nonorthogonal

basis ϕ_b.[52] However, it does not conserve the total density of states, i.e., $\mathrm{Tr}(GS) \neq \mathrm{Tr}(SGS)$. Equation (A5) is equivalent to the more symmetrical expression given by Gyemant and Kelly[52] only when considering the trace (total DOS), since $\mathrm{Tr}(SGS)=\mathrm{Tr}(S^{1/2}GSS^{1/2})$.

From Eq. (A5), it can be seen that some of the nondiagonal elements of $\tilde{G}=GS$ enter in the calculation of PDOS_{ϕ_b} through S in the multiplication $S(GS)=S\tilde{G}$. This is to compensate for the contributions to $\tilde{\phi}_b$ of nonorthogonal functions other than ϕ_b in Eq. (A2).

Nonorthogonal basis are usually constructed to resemble true orthogonal atomic orbitals, i.e., the overlap matrix is very close to the identity, $S \approx \mathbf{1}$, which closes the difference between the definitions in Eqs. (A4) and (A5). This is especially true for the single-zeta basis set as used in this study. Additionally, the linear transformation $S^{1/2}$ produces the orthogonal set that has the greatest least-squares similarity to the original nonorthogonal set.

The small difference between the two definitions for PDOS becomes negligible when summing over atoms or fragments. Figure 10 compares the PDOS on the sulfur atoms of junction 1, previously shown in Fig. 6; in other words, it shows the PDOS summed over all the basis functions that belong to the sulfur atoms. As it can be seen in the figure, even when projecting on only two atoms in a zoomed-in energy range, the differences between the definitions in Eqs. (A4) and (A5) are negligible. Therefore, we have that

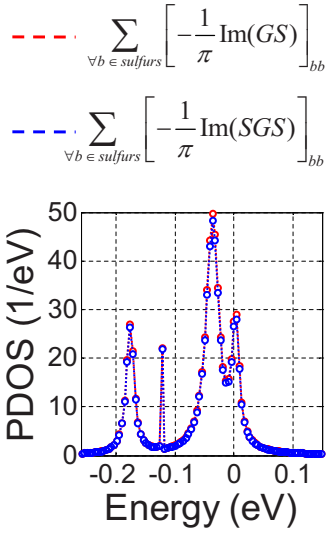

FIG. 10. (Color online) Comparison between DOSs projected on the sulfur atoms of junction 1. The red curve projects on an orthogonalized basis set while the blue curve a nonorthogonal set.

$$\mathrm{PDOS}_{\mathrm{fragment}} \equiv \sum_{\forall\, b \in \mathrm{fragment}} \left[-\frac{1}{\pi}\mathrm{Im}(GS)\right]_{bb} \approx \sum_{\forall\, b \in \mathrm{fragment}} \left[-\frac{1}{\pi}\mathrm{Im}(SGS)\right]_{bb}. \quad \text{(A6)}$$

[1] L. A. Agapito and H. P. Cheng, J. Phys. Chem. C **111**, 14266 (2007).
[2] A. R. Rocha, V. M. Garcia-Suarez, S. W. Bailey, C. J. Lambert, J. Ferrer, and S. Sanvito, Nat. Mater. **4**, 335 (2005).
[3] I. Rungger and S. Sanvito, Phys. Rev. B **78**, 035407 (2008).
[4] Z. J. Donhauser, B. A. Mantooth, K. F. Kelly, L. A. Bumm, J. D. Monnell, J. J. Stapleton, D. W. Price, A. M. Rawlett, D. L. Allara, J. M. Tour, and P. S. Weiss, Science **292**, 2303 (2001).
[5] L. A. Agapito, E. J. Bautista, and J. M. Seminario, Phys. Rev. B **76**, 115316 (2007).
[6] M. A. Reed, J. Chen, A. M. Rawlett, D. W. Price, and J. M. Tour, Appl. Phys. Lett. **78**, 3735 (2001).
[7] N. Gergel, N. Majumdar, K. Keyvanfar, N. Swami, L. R. Harriott, J. C. Bean, G. Pattanaik, G. Zangari, Y. Yao, and J. M. Tour, J. Vac. Sci. Technol. A **23**, 880 (2005).
[8] J. M. Seminario, Y. F. Ma, L. A. Agapito, L. M. Yan, R. A. Araujo, S. Bingi, N. S. Vadlamani, K. Chagarlamudi, T. S. Sudarshan, M. L. Myrick, P. E. Colavita, P. D. Franzon, D. P. Nackashi, L. Cheng, Y. X. Yao, and J. M. Tour, J. Nanosci. Nanotechnol. **4**, 907 (2004).
[9] J. G. Kushmerick, J. Naciri, J. C. Yang, and R. Shashidhar, Nano Lett. **3**, 897 (2003).
[10] L. T. Cai, H. Skulason, J. G. Kushmerick, S. K. Pollack, J. Naciri, R. Shashidhar, D. L. Allara, T. E. Mallouk, and T. S. Mayer, J. Phys. Chem. B **108**, 2827 (2004).
[11] J. K. N. Mbindyo, T. E. Mallouk, J. B. Mattzela, I. Kratochvilova, B. Razavi, T. N. Jackson, and T. S. Mayer, J. Am. Chem. Soc. **124**, 4020 (2002).
[12] J. Chen, M. A. Reed, A. M. Rawlett, and J. M. Tour, Science **286**, 1550 (1999).
[13] N. Gergel-Hackett, N. Majumdar, Z. Martin, N. Swami, L. R. Harriott, J. C. Bean, G. Pattanaik, G. Zangari, Y. Zhu, I. Pu, Y. Yao, and J. M. Tour, J. Vac. Sci. Technol. A **24**, 1243 (2006).
[14] N. Majumdar, N. Gergel-Hackett, J. C. Bean, L. R. Harriott, G. Pattanaik, G. Zangari, Y. Yao, and J. M. Tour, J. Electron. Mater. **35**, 140 (2006).
[15] A. A. Dhirani, R. W. Zehner, R. P. Hsung, P. Guyot Sionnest, and L. R. Sita, J. Am. Chem. Soc. **118**, 3319 (1996).
[16] Y. H. Kim, J. Tahir-Kheli, P. A. Schultz, and W. A. Goddard, Phys. Rev. B **73**, 235419 (2006).
[17] J. Taylor, M. Brandbyge, and K. Stokbro, Phys. Rev. B **68**, 121101(R) (2003).
[18] L. Romaner, G. Heimel, and E. Zojer, Phys. Rev. B **77**, 045113 (2008).
[19] M. Q. Long, K. Q. Chen, L. Wang, B. S. Zou, and Z. Shuai, Appl. Phys. Lett. **91**, 233512 (2007).
[20] S. Sanvito, C. J. Lambert, J. H. Jefferson, and A. M. Bratkovsky, Phys. Rev. B **59**, 11936 (1999).
[21] P. M. Haney, D. Waldron, R. A. Duine, A. S. Nunez, H. Guo, and A. H. MacDonald, Phys. Rev. B **75**, 174428 (2007).
[22] C. Zhang, X. G. Zhang, P. S. Krstic, H. P. Cheng, W. H. Butler, and J. M. MacLaren, Phys. Rev. B **69**, 134406 (2004).

[23] B. Bonferroni, A. Ferretti, A. Calzolari, A. Ruini, M. J. Caldas, and E. Molinari, Nanotechnology **19**, 285201 (2008).
[24] V. Timoshevskii, Y. Q. Ke, H. Guo, and D. Gall, J. Appl. Phys. **103**, 113705 (2008).
[25] S. Alkis, P. Jiang, L. L. Wang, A. E. Roitberg, H. P. Cheng, and J. L. Krause, J. Phys. Chem. C **111**, 14743 (2007).
[26] L. Miao and J. M. Seminario, J. Chem. Phys. **126**, 184706 (2007).
[27] J. J. Stapleton, P. Harder, T. A. Daniel, M. D. Reinard, Y. X. Yao, D. W. Price, J. M. Tour, and D. L. Allara, Langmuir **19**, 8245 (2003).
[28] J. M. Soler, E. Artacho, J. D. Gale, A. Garcia, J. Junquera, P. Ordejon, and D. Sanchez-Portal, J. Phys.: Condens. Matter **14**, 2745 (2002).
[29] J. P. Perdew, K. Burke, and M. Ernzerhof, Phys. Rev. Lett. **77**, 3865 (1996).
[30] E. Artacho, D. Sanchez-Portal, P. Ordejon, A. Garcia, and J. M. Soler, Phys. Status Solidi B **215**, 809 (1999).
[31] J. Junquera, O. Paz, D. Sanchez-Portal, and E. Artacho, Phys. Rev. B **64**, 235111 (2001).
[32] H. J. Monkhorst and J. D. Pack, Phys. Rev. B **13**, 5188 (1976).
[33] P. S. Krstic, X. G. Zhang, and W. H. Butler, Phys. Rev. B **66**, 205319 (2002).
[34] X. G. Zhang, P. S. Krstic, and W. H. Butler, Int. J. Quantum Chem. **95**, 394 (2003).
[35] N. W. Ashcroft and N. D. Mermin, *Solid State Physics* (Holt, New York, 1976).
[36] R. B. Leighton, Rev. Mod. Phys. **20**, 165 (1948).
[37] M. Born and T. von Karman, Phys. Z. **14**, 15 (1913).
[38] M. Born and T. von Karman, Phys. Z. **13**, 297 (1912).
[39] C. Caroli, R. Combesco, P. Nozieres, and D. Saintjam, J. Phys. C **4**, 916 (1971).
[40] G. H. Yang, Y. L. Qian, C. Engtrakul, L. R. Sita, and G. Y. Liu, J. Phys. Chem. B **104**, 9059 (2000).
[41] G. Heimel, L. Romaner, E. Zojer, and J. L. Bredas, Nano Lett. **7**, 932 (2007).
[42] A. Rochefort, R. Martel, and P. Avouris, Nano Lett. **2**, 877 (2002).
[43] P. Puschnig and C. Ambrosch-Draxl, Monatsch. Chem. **139**, 389 (2008).
[44] P. Puschnig and C. Ambrosch-Draxl, Phys. Rev. B **60**, 7891 (1999).
[45] W. Mönch, *Semiconductor Surfaces and Interfaces* (Springer, Berlin, 2001).
[46] R. C. Hoft, M. J. Ford, and M. B. Cortie, Chem. Phys. Lett. **429**, 503 (2006).
[47] Y. Q. Xue and M. A. Ratner, Phys. Rev. B **68**, 115407 (2003).
[48] S. H. Ke, H. U. Baranger, and W. T. Yang, J. Chem. Phys. **122**, 074704 (2005).
[49] M. P. L. Sancho, J. M. L. Sancho, and J. Rubio, J. Phys. C **18**, 1803 (1985).
[50] X. Zhang, L. Fonseca, and A. A. Demkov, Phys. Status Solidi B **233**, 70 (2002).
[51] J. J. Palacios, A. J. Pérez-Jiménez, E. Louis, E. SanFabián, J. A. Vergés, and Y. García, in *Computational Chemistry: Reviews of Current Trends*, edited by J. Leszcynski (World Scientific, Singapore, 2005), Vol. 9.
[52] I. Gyemant and M. J. Kelly, J. Phys. C **11**, L193 (1978).